NExt ApplicationS of Quantum Computing

D4.9: Benchmarking Report

Document Properties

Contract Number	951821
Contractual Deadline	31-10-2024 (M50)
Dissemination Level	Public
Nature	Report
Editors	Jan Reiner, HQS Quantum Simulations
Authors	Arseny Kovyrshin, Data Science and Modeling, Pharmaceutical Sciences, R&D, AstraZeneca, Gothenburg, Sweden Giorgio Silvi, HQS Quantum Simulations Jan Reiner, HQS Quantum Simulations Venkatesh Kannan, ICHEC
Reviewers	Vedran Dunjko, Leiden University Wassil Sennane, TotalEnergies
Date	25-10-2024
Keywords	Quantum computing, VQE, Pre-Born-Oppenheimer, Nuclear-Electronic Orbitals (NEO), measurement optimization, shadow spectroscopy, Bayesian statistics, enhanced sampling, n-representability, CO_2 recapture, graphene
Status	Final
Release	1.0

This project has received funding from the European Union's Horizon 2020 research and innovation programme under Grant Agreement No. 951821

History of Changes

Release	Date	Author, Organisation	Description of Changes
0.1	23-10-2024	Arseny Kovyrshin, Data Science and Modeling, Pharmaceutical Sciences, R&D, AstraZeneca, Gothenburg, Sweden; Giorgio Silvi and Jan Reiner, HQS Quantum Simulations; Venkatesh Kannan, ICHEC	First version for review
0.2	25-10-2024	Arseny Kovyrshin, Data Science and Modeling, Pharmaceutical Sciences, R&D, AstraZeneca, Gothenburg, Sweden; Giorgio Silvi and Jan Reiner, HQS Quantum Simulations; Venkatesh Kannan, ICHEC	Implemented changes suggested by Vedran Dunjko
1.0	25-10-2024	Arseny Kovyrshin, Data Science and Modeling, Pharmaceutical Sciences, R&D, AstraZeneca, Gothenburg, Sweden; Giorgio Silvi and Jan Reiner, HQS Quantum Simulations; Venkatesh Kannan, ICHEC	Final version after implementing changes suggested by Wassil Sennane

Table of Contents

1 Executive Summary

This document is a continuation of deliverable D4.3 of the NEASQC project and is concerned with benchmarking the applications for quantum computing researched and implemented within the quantum chemistry work package of the project.

In D4.3 we reported assessments contributed from three of the partners within the work package:

AstraZeneca presented a benchmarking study for chemical reactivity with our previously implemented Pre-Born-Oppenheimer quantum computing computational package [1], where the showcase was the reaction of water hydrogenation.

HQS Quantum Simulations demonstrated a performance analysis of their implemented variational algorithms [1], comparing a Variational Quantum Eigensolver (VQE) implementing UCCSD, an Adaptive Variational Quantum Eigensolver (AdaptVQE) using UCCSD, a variational Hamiltonian ansatz (VHA), and a variational imaginary time evolution (VITE) with two-local ansatz [2–5].

TotalEnergies estimated the feasibility to execute families of Hardware Efficient (HE) quantum computing ansatzes and quantum Unitary Coupled Cluster (qUCC) ansatzes on (noisy) near-term quantum computers, applied to a calculation of the ground state energy of strained benzene [6, 7].

In this report, that constitutes deliverable D4.9 of the NEASQC project, we extend on these contributions:

In Chap. 2, AstraZeneca extended their investigations to the interaction of CO_2 with a hydrogen radical using the Nuclear-Electronic Orbital (NEO) Quantum Computing Framework [8, 9], with a specific focus on simulating the reduction of CO_2.

In Chap. 3, HQS Quantum Simulations focuses here on the evaluation of methods to improve quantum measurements, one utilizing shadow measurement in the context of spectroscopy [10], one based on enhanced sampling using Bayesian statistics [11], and one based on projecting the result to fulfill so-called n-representability constraints which may be violated in a noisy quantum computation [12]. This is reported on in more detail in deliverable D4.7, with software implementations available on the NEASQC GitHub [1].

In Chap. 4, TotalEnergies continued their studies regarding benzene to a calculation of a system of graphene and a CO_2 molecule using a VQE approach, which could be used in the context of understanding recapture processes of carbon dioxide. Similar to above, this study is reported on in more detail in deliverable D4.8, with related software found on the NEASQC GitHub [13].

Finally, in Chap. 5, ICHEC gives an overview of the software tool `KraChem` which was developed within the NEASQC project. The tool is designed to automatically fragment molecular systems into smaller subsystems, allowing breaking down large problems into subproblems, making them digestible for NISQ computations. This automatic subspace generation was reported on earlier in detail in deliverable D4.6, and is available on the NEASQC GitHub as well [14].

2 CO_2 Reduction via Hydrogen Radical Collision

This chapter investigates the interaction of CO_2 with a hydrogen radical using the Nuclear-Electronic Orbital (NEO) Quantum Computing Framework [8, 9], with a specific focus on simulating CO_2 reduction. The proton from the hydrogen radical is treated quantum mechanically, and additional momentum is applied to the proton in the direction of the collision with CO_2, mimicking high-pressure conditions or the collision of accelerated hydrogen radicals. We will explain how the additional momentum modifies the proton's kinetic energy, introduces coupling terms, and why potential energy terms remain unchanged. We also provide explanations summarizing the Hamiltonian's components.

2.1 System Setup and Computational Methods

The system studied involves the following components: *Reactants* include carbon dioxide (CO_2) molecule and a hydrogen radical ($H^{\cdot}$); *Product* is a formate radical ($HCOO^{\cdot}$); and *Transition State* where the hydrogen radical starts interacting with CO_2 (highest point in reaction pathway). The initial structures for the reactants, transition state, and product were optimized using the MP2 method with the CC-pVDZ basis set [15] for the electronic orbitals available in GAMESS-US software package [16]. The optimized structures are shown in Fig. 1. These optimized structures

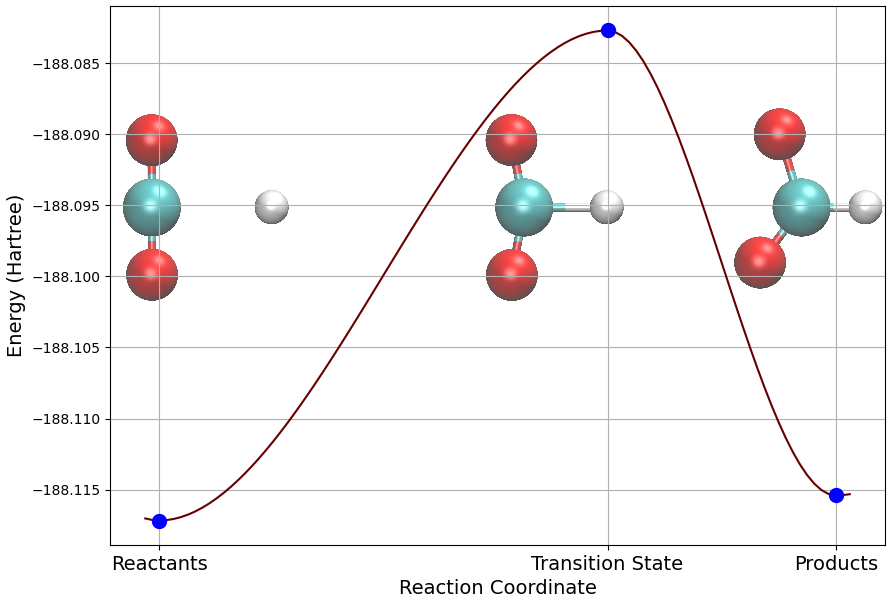

***Figure 1**: Optimized structures of the reactants (CO_2 and $H^{\cdot}$), transition state, and product ($HCOO^{\cdot}$) as obtained from MP2/CC-pVDZ calculations. The potential energy surface was fitted using PCHIP to visually represent the reaction path.*

were then used for generation of the Qubit Hamiltonian in the NEO Quantum Computing Framework. Within this framework both the electrons and the proton are treated quantum mechanically, allowing for simultaneous treatment of electron and proton degrees of freedom. For the protonic orbitals, the PB4-F2 Cartesian basis set [17] was employed to accurately describe the quantum behavior of the proton. A minimal active space was created, consisting of 4 active orbitals for electrons and 6 active orbitals for protons, representing the key interactions between the particles. This approach enables a more accurate description of proton transfer processes within the reaction mechanism.

The energies computed Fermionic AdaptVQE method [18] for Reactants, Transition State, and Products are shown in Fig. 1. These values correspond to the important reaction points, providing insight into the nuclear and electronic interactions across the reaction pathway. A spline interpolation of the reaction potential energy surface (PES) was performed using the Piecewise Cubic Hermite Interpolating Polynomial (PCHIP) method, which provides a smooth fit for the calculated energies along the reaction pathway.

2.2 NEO Hamiltonian and Additional Momentum

In the NEO approach, the Hamiltonian for the system includes three main components: The electronic Hamiltonian ($\hat{H}_e$), the protonic Hamiltonian ($\hat{H}_p$), and the electron-proton coupling Hamiltonian ($\hat{H}_{ep}$)

$$\hat{H}_{NEO} = \hat{H}_e + \hat{H}_p + \hat{H}_{ep}.$$

The electronic Hamiltonian describes the motion and interaction of the electrons in the system

$$\hat{H}_e = \sum_{ij} h_{ij} a_i^\dagger a_j + \frac{1}{2} \sum_{ijkl} g_{ijkl} a_i^\dagger a_j^\dagger a_k a_l,$$

where h_{ij} are one-electron integrals (kinetic energy and electron-nuclei attraction), g_{ijkl} are two-electron integrals (electron-electron repulsion), $a_i^\dagger$ and a_j are electron creation and annihilation operators. The protonic Hamiltonian has a similar form and reads as follows

$$\hat{H}_p = \sum_{mn} T_{mn} b_m^\dagger b_n + \frac{1}{2} \sum_{mnop} V_{mnop} b_m^\dagger b_n^\dagger b_o b_p$$

where T_{mn} are the one-proton integrals (kinetic energy and proton-nuclear attraction), V_{mnop} are proton-proton repulsion terms, $b_{m,n}^\dagger$ and $b_{o,p}$ are proton creation and annihilation operators. The interaction between the electrons and the proton is accounted for by the electron-proton coupling Hamiltonian

$$\hat{H}_{ep} = \sum_{ij,mn} C_{ijmn} a_i^\dagger a_j b_m^\dagger b_n$$

where C_{ijmn} represents the electron-proton interaction integrals.

We now modify the Hamiltonian to include the effect of an additional momentum Δp to the proton, mimicking an accelerated hydrogen radical collision with CO_2. The *momentum boost operator* $\hat{U}(\Delta p) = e^{i\frac{\Delta p \cdot \hat{r}}{\hbar}}$ is used to add momentum Δp to the proton without changing its position. This operator shifts the proton's momentum but leaves the position space unchanged. When the boost operator is applied to the proton's Hamiltonian, it modifies the kinetic energy and introduces new coupling terms between the proton's original momentum and the added momentum

$$\hat{H}_p^{boosted} = \sum_{mn} \left(T_{mn} + \delta_{mn} \frac{\Delta p^2}{2m_p} \right) b_m^\dagger b_n + \sum_{mn} \left(\Delta p \cdot \frac{P_{mn}}{m_p} \right) b_m^\dagger b_n.$$

The first term represents the proton's kinetic energy with the added constant Δp^2 term. The second term introduces off-diagonal coupling between the proton's original momentum and the added momentum. While the boost operator introduces new terms in the kinetic energy and momentum-dependent interactions, it does not modify the potential energy terms in the Hamiltonian. This is because the boost operator only shifts momentum and has no direct effect on position. Potential energy terms are typically functions of the position operator $\hat{r}$, such as $\hat{V}(\hat{r})$. Since the boost operator commutes with the position operator (i.e., it does not change the proton's position),

$$\hat{U}^\dagger(\Delta p) \hat{V}(\hat{r}) \hat{U}(\Delta p) = \hat{V}(\hat{r}),$$

applying the boost operator to the potential energy term does not introduce any new terms. Thus including the modified proton Hamiltonian, the full NEO Hamiltonian with additional momentum becomes

$$\hat{H}_{total}^{boosted} = \sum_{mn} \left(T_{mn} + \delta_{mn} \frac{\Delta p^2}{2m_p} \right) b_m^\dagger b_n + \hat{H}_e + \sum_{mn} \left(\Delta p \cdot \frac{P_{mn}}{m_p} \right) b_m^\dagger b_n + \hat{H}_{ep}.$$

2.3 Impact of Added Momentum on Reaction Pathways

In the hydrogenation of CO_2, we investigate the effect of imparting additional momentum to the proton on the reaction pathway. The momentum is applied in the direction of the proton's collision with the carbon atom of the CO_2 molecule, simulating a high-energy collision event. This added momentum increases the initial kinetic energy of the proton, influencing its ability to overcome the activation energy required to reach the transition state (TS). The momenta

applied to the proton are

$$\Delta p = [0, 2.5, 5.0, 7.0, 10.0, 12.5, 15.0] \text{ a.u.}$$

The energies along the reaction pathway were computed using our NEO quantum computing framework, as discussed in detail in deliverable D4.4. The calculation of these energies was done using the Fermionic Adapt-VQE ansatz, which optimizes the quantum state by adaptively selecting fermionic operators that efficiently describe the system's correlation. The Adapt-VQE method was particularly useful in capturing the complex electron-proton interactions in the NEO framework, enabling the precise evaluation of energies at different points along the reaction coordinate. The reaction pathways, showing the potential energy surface (PES) from reactants to products, were fitted using the PCHIP method. Figure 2 illustrates the reaction pathways with no added momentum ($\Delta p = 0$) as well as the energy shift caused by increasing the proton's momentum.

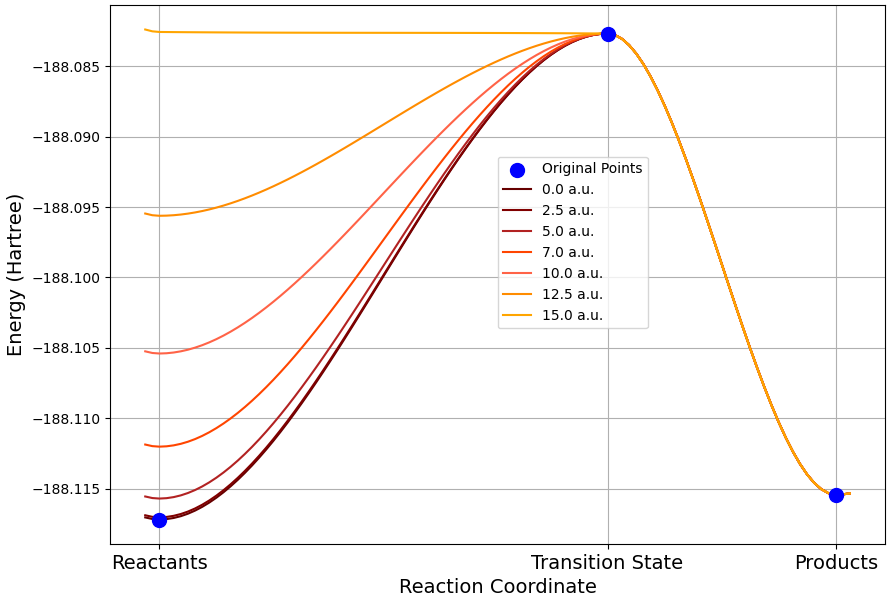

***Figure 2**: Reaction pathways for different proton momenta ($\Delta p = [0, 2.5, 5.0, 7.0, 10.0, 12.5, 15.0]$ a.u.), fitted using the PCHIP method. The transition state (TS) represents the highest energy point along the pathway. For $\Delta p = 15.0$ a.u., the proton's initial energy is nearly equal to the TS energy, significantly facilitating the reaction.*

As momentum is added to the proton, its initial kinetic energy increases, raising the total energy at the start of the reaction. The kinetic energies for different proton momenta are presented in Table 1 (next section). For $\Delta p = 15.0$ a.u., the initial kinetic energy is approximately 2.672×10^{-19} J (or 0.06131 Hartree). As seen in Figure 2, as the proton's momentum increases, the total energy progressively approaches the transition state energy. For $\Delta p = 15.0$ a.u., the Reactant's energy is almost equal to the transition state energy. This suggests that at such a high momentum, the proton can overcome the reaction barrier. These results highlight the potential of using momentum-driven approaches to facilitate reactions involving high activation barriers, such as the hydrogenation of CO_2.

2.4 Pressure and Temperature Evaluations

In this section, we calculate the pressures and corresponding temperatures resulting from the additional momentum imparted to the proton during the collision with CO_2 in the hydrogenation reaction. The kinetic energy E_k of the proton is calculated from its momentum Δp using the classical relation

$$E_k = \frac{(\Delta p)^2}{2m_p}$$

where Δp is the momentum of the proton in atomic units (a.u.), m_p is the mass of the proton, $m_p = 1.6726 \times 10^{-27}$ kg. To convert momentum from atomic units to SI units (kg m/s), we use

$$1\,\text{a.u.} = 1.9929 \times 10^{-24}\,\text{kg m/s}$$

The kinetic energy of the proton is related to the temperature of the system using the equipartition theorem

$$E_k = \frac{3}{2} k_B T$$

where $k_B = 1.380649 \times 10^{-23}$ J/K is the Boltzmann constant and T is the temperature of the system in Kelvin (K). Rearranging this formula to solve for temperature T:

$$T = \frac{2E_k}{3k_B}.$$

Then the pressure of the system is calculated using the ideal gas law

$$P = nk_B T$$

where $n = 2.6868 \times 10^{25}$ particles/m^3 is the number density. The table below presents the calculated temperatures and pressures corresponding to each momentum value.

Momentum (a.u.)	Kinetic Energy (J)	Temperature (K)	Pressure (Pa)	Pressure (atm)
2.5	7.424×10^{-21}	3593	1.333×10^5	1.32
5.0	2.969×10^{-20}	14373	5.334×10^5	5.26
7.0	5.810×10^{-20}	28127	1.044×10^6	10.3
10.0	1.188×10^{-19}	57562	2.136×10^6	21.1
12.5	1.855×10^{-19}	89930	3.338×10^6	32.9
15.0	2.672×10^{-19}	129127	4.790×10^6	47.3

***Table 1**: Kinetic energies, temperatures, and pressures for different proton momenta in the CO_2 hydrogenation reaction.*

2.5 Conclusion

The temperatures and pressures resulting from the high momenta imparted to the proton reach extreme values. For instance, the temperature corresponding to $\Delta p = 15$ a.u. is approximately 1.291×10^5 K, and the pressure is around 47.3 atm. Instead of relying on extremely high temperatures, which lead to highly ionized particles and uncontrolled reactions, a more feasible approach would be to utilize a cryogenic shockwave setup. In this method, the system is kept at low temperatures while localized high-energy collisions are induced by shockwaves, avoiding excessive ionization and enabling more controlled chemical reactions. Our computational setup, which incorporates additional momentum in the protonic part, is designed to model exactly these conditions, simulating the energy transfer and reaction dynamics that occur in a cryogenic shockwave environment.

The generation of shockwaves at cryogenic temperatures can be achieved through several potential methods. Mechanical impact devices or pneumatic systems can generate controlled shockwaves, while laser-driven techniques or explosive devices could provide rapid energy input to specific regions, creating the necessary high-pressure conditions. Alternatively, particle accelerators could be used to impart high momentum to protons before they collide with CO_2, replicating the high-energy collisions modeled in our system. These techniques, when applied in a cryogenic environment, would maintain the overall system temperature low while enabling localized high-energy proton-CO_2 interactions, closely mimicking the dynamics predicted by our quantum-based calculations.

3 Measuement Optimization

After focussing on the evolution of quantum states in deliverable D4.3, here we will present a performance analysis of methods to optimize the measurement of quantum states. It is a widely discussed problem that the number of measurements needed to obtain an accurate result is a serious resource strain in NISQ computing.

In the sections we present three methods trying to gain the most information out of a limited number measurements as possible. One method is utilizing shadow measurement in the context of spectroscopy, one is based on enhanced sampling using Bayesian statistics, and one is based on projecting the result to fulfill so-called n-representability constraints which may be violated in a noisy quantum computation.

The text in this chapter is a very brief summary of the results, where one can find a more detailed report in deliverable D4.7, and software implementations available on the NEASQC GitHub [1]. Furthermore, we would like to highlight that the n-representability projection methods was extensively studied, in particular in the presence of noise, in a scientific publication of ours [12].

3.1 Shadow spectroscopy

Determining energy spectra of quantum systems is a fundamental task in quantum physics and chemistry. Methods like quantum phase estimation require significant quantum resources, making them challenging to implement on near-term quantum devices.

Shadow spectroscopy [10] is a quantum algorithm designed to estimate energy differences (gaps) in a system's Hamiltonian by analyzing the time evolution of quantum states. It requires relatively few quantum resources (no ancilla qubits, very few shots) and demonstrates resilience to noise, making it well-suited for noisy intermediate-scale quantum (NISQ) devices. The method exploits the fact that observable quantities evolve over time according to the system's energy differences, which can be extracted through harmonic analysis of the measured signals. It leverages classical shadows [19] – a technique based on randomized measurements – to access a broad set of observables that encode information about the energy spectrum.

As a benchmarking case, we provide a jupyter notebook in our repository [1] where we apply shadow spectroscopy to estimate the energy spectrum of a trimethylenebenzene (TMB) molecule, modeled by the spin Hamiltonian:

$$H_S = 3(\epsilon + J - K) + \frac{3J_S}{4} - \frac{J_S}{4}\left(\sigma_1\sigma_2 + \sigma_1\sigma_3 + \sigma_2\sigma_3\right), \tag{3.1}$$

where σ_i are Pauli operators acting on qubit i, and ϵ, J, K, and J_S are system-specific constants.

In our simulation (see Figure 3), we perform shadow measurements with two different numbers of shots per Trotter step: 10 and 1000 shots. Note, that even 1000 shots is few in the context of quantum computing where one would estimate expectation values; 10 measurements to obtain the estimate of an expectation value would yield a highly inaccurate estimate. Here, the resulting spectra successfully identify a peak at 0.029 $(= 3/2J_S)$ Hartree for both simulations, corresponding to the energy gap of the Hamiltonian.

In conclusion, shadow spectroscopy provides an efficient and practical approach to estimating energy gaps in quantum systems using NISQ devices. By harnessing classical shadows and time-evolution techniques, it overcomes limitations of traditional methods, requiring extremely few quantum resources and offering resilience to noise. This method opens pathways for studying complex quantum systems and advances the capabilities of early quantum hardware.

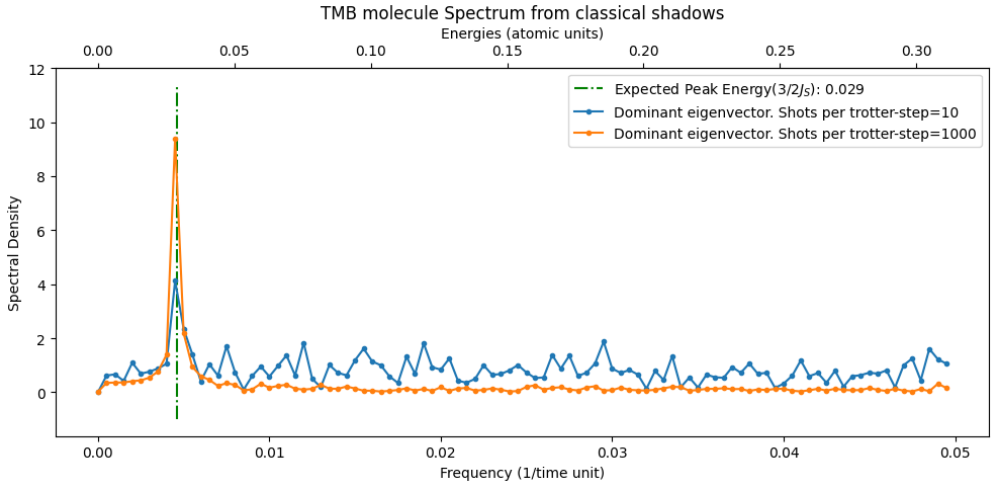

***Figure 3**: Spectral estimation of the TMB molecule using shadow spectroscopy with 10 and 1000 shots per Trotter step. A peak at 0.029 Hartree corresponds to the energy gap of interest.*

3.2 Enhanced sampling

In this section, we give an overview of our investigated method of enhanced sampling based on Bayesian statistics.

The enhanced sampling method proposed in Ref. [11] is a technique that maximizes the statistical power of noisy quantum devices. This method is inspired by quantum-enhanced metrology, phase estimation, and the more recent "alpha-VQE" and aims to improve the efficiency of quantum amplitude estimation.

In standard sampling, as used in Variational Quantum Eigensolver (VQE), the estimation process is insensitive to small deviations in the expectation value, leading to low information gain from measurement outcomes when increasing to higher number of measurements. This results in a high runtime cost for interesting practical problems.

Enhanced sampling addresses this issue by engineering likelihood functions that increase the rate of information gain, thereby reducing the runtime of amplitude estimation. The method involves preparing an ansatz state, applying an operator, adding a phase shift about the ansatz state, and then measuring the operator. The phase shift can be achieved by performing the inverse of the ansatz circuit, then a phase shift about the initial state, and then re-applying the ansatz circuit. An example with 1 layer is shown in Fig. 4

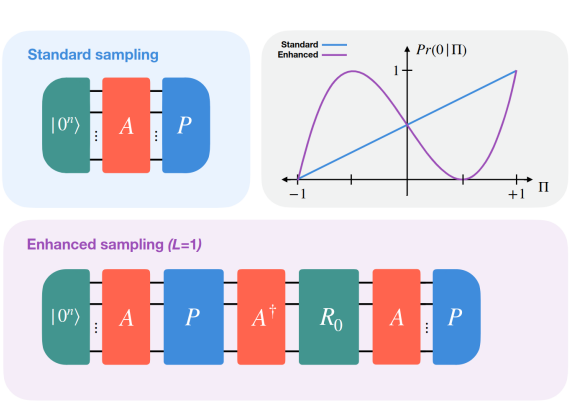

***Figure 4**: Circuit for standard sampling vs enhanced sampling. Source [1].*

In Ref. [11], the Engineered Likelihood Function (ELF) is used to estimate the parameters of a quantum circuit. The ELF maps the parameters of the quantum circuit to a likelihood value, which measures how well the circuit fits the data. It is constructed by defining a prior distribution over the parameters, and then using Bayes' rule to compute the posterior distribution given the data. The likelihood function is then defined as the marginal distribution of the data given the parameters. The ELF is used to perform maximum likelihood estimation of the parameters, which involves

finding the parameters that maximize the likelihood function. This is done using a classical optimization algorithm, such as gradient descent.

In our work [1], we have chosen to implement an alternative approach where, for a given ansatz and some pre-sampling, the algorithm selects between two enhanced-circuit with different number of layers, instead of using the Engineered Likelihood Function (ELF). This method involves selecting the enhanced circuit with the highest Fisher information to be used for sampling. Fisher information is a measure of the amount of information that an observable random variable carries about an unknown parameter, and maximizing it can lead to more efficient sampling.

By selecting the circuit with the highest Fisher information, we aim to maximize the information gain from each measurement, thereby reducing the total number of measurements needed. This approach is more practical for our purposes than implementing the ELF, as it does not require the time-consuming adaptive scheme to be applied at every shot.

3.2.1 Results

In our repository, we offer a demonstrative notebook that showcases the capabilities of the algorithm. Specifically, given a Hamiltonian and an ansatz, we evaluate the root mean square error of the measured energy relative to the exact energy. As illustrated in Fig. 5, following an initial shared presampling phase (standard), we compare the performance of the enhanced sampling technique to that of standard sampling as additional measurements are conducted in both scenarios. In a noiseless environment, it is evident that the enhanced sampling technique outperforms standard sampling. However, this improvement is accompanied by a rise in complexity and, more significantly, an increase in circuit depth. The latter is particularly disadvantageous in noisy environments such as those experienced by Near-Term Intermediate-Scale Quantum (NISQ) devices. This drawback is evident in the case of the noisy 3-qubit system depicted in Fig. 5d. Here, the performance of enhanced sampling deteriorates to a point below that of standard sampling.

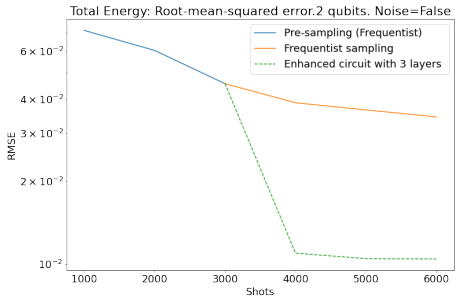

(a) 5 Runs on a 2-qubit EfficientSU2 ansatz on a noiseless simulator.

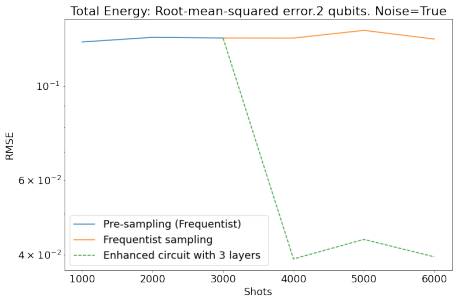

(b) 5 Runs on a 2-qubit EfficientSU2 ansatz on a noisy simulator.

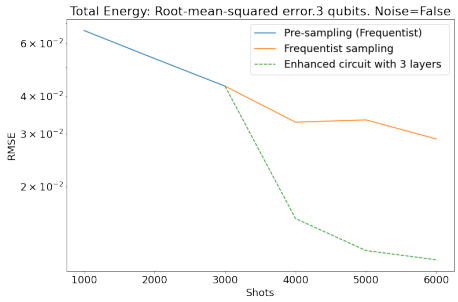

(c) 5 Runs on a 3-qubit EfficientSU2 ansatz on a noiseless simulator.

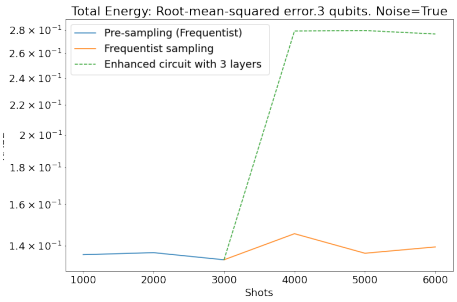

(d) 5 Runs on a 3-qubit EfficientSU2 ansatz on a noisy simulator.

***Figure 5**: Root mean square errors for various experimental setups and configurations.*

While the ELF formalism offers a promising method for enhancing the power of sampling on quantum devices, its practical implementation can be challenging due to the time required for the adaptive scheme. The two enhanced-circuit choice offers a practical alternative that can reduce the number of measurements and runtime compared to

standard sampling, making it a promising approach for the implementation of quantum algorithms in practical applications.

3.3 Post-processing noisy quantum computations utilizing n-representability constraints

In this section, we consider a method for improving the results of a noisy quantum computation, e.g., obtained from a NISQ device. We will describe here briefly how the method works in the following theory subsection and show some selected results in the subsequent subsection. A thorough analysis of the approach, including a detailed explanation of the method and the motivation behind it, as well extensive numerical data and a discussion of its caveats are given in our publication on this subject [12].

We would like to find the internal energy given by the expectation value of the Hamiltonian,

$$\langle H \rangle = E_0 + \sum_{ij} t_{ij} ({}^1D_{ij}) + \sum_{ijkl} V_{ijkl} ({}^2D_{ijkl}), \tag{3.2}$$

with the annihilation (creation) operators $c_i^{(\dagger)}$ of an electron in orbital i, the energy offset E_0, the one- and two-electron integrals t_{ij} and V_{ijkl}, as well as the one-particle RDM ${}^1D_{ij} = \langle c_i^\dagger c_j \rangle$, and the two-particle RDM ${}^2D_{ijkl} = \langle c_i^\dagger c_j^\dagger c_l c_k \rangle$.

If ${}^1D$ and ${}^2D$ of the ground state are obtained from a quantum computation on a NISQ device, they are obscured by decoherence and shot noise. We assume, that the dominating noise source is decoherence, and in this case, the calculated energy would be higher then the actual ground state energy.

One can mitigate this error and the statistical variance from shot noise by imposing constraints that the RDMs need to fulfill: From the anti-commutation relations of the fermionic operators, on can derive that they are Hermitian and obey a certain set of anti-symmetry relations. These constraints are usually fulfilled in a quantum computation by simply calculating only a minimal necessary set of matrix elements and reconstructing the rest through the Hermiticity and anti-symmetry constraints. Less trivial are the constraints that the RDMs need to be positive semi-definite and the trace depend on the particle number n via $\mathrm{tr}({}^1D) = n$, and $\mathrm{tr}({}^2D) = n(n-1)$.

We impose these by projecting; we find the RDM that fulfills these conditions and is, in some norm, closest to the RDM calculated on the quantum computer. Furthermore, one can transform the one- and two-particle RDMs into the hole and particle-hole sector. This means we can transform to the one- and two-hole RDMs, ${}^1Q_{ij} = \langle c_i c_j^\dagger \rangle$ and ${}^2Q_{ijkl} = \langle c_i c_j c_l^\dagger c_k^\dagger \rangle$, and the particle-hole RDM ${}^2G_{ijkl} = \langle c_i^\dagger c_j c_l^\dagger c_k \rangle$. In these sectors, the same constraints hold (where the trace now depends not only on the number of electrons in the system, but also the number of holes). We perform the projection of the measured RDMs in all three sectors, and return the energetically best of these results, as we assume the noise to be dominated by decoherence.

3.3.1 Results

To showcase the performance of the method, we give here examples of a ground state calculation of H_2 under the influence of damping noise in Fig. 6, and under the influence of damping noise and shot noise in Fig. 7. For damping noise only we look at the energy difference of the calculation with respect to the actual ground state energy, as well as the final state fidelity. When including shot noise, we looked at the energy difference with respect to the ground state and the measurement variance.

In Fig. 6, one can see the improvement of the energy difference of almost an order of magnitude. Note also the general improvement in fidelity, but obtaining the best energy does not guarantee the best fidelity.

In Fig. 7, we should mention that *Best* is strictly lower than other projections in this case, as here we average over 100 repetitions of the same measurement with different shot noise, to obtain a variance, and in each repetition different projections might lead to the energetically best result. The plot shows significant improvement of the energy difference, but also – and arguably more importantly – the reduction of the measurement variance up to two orders of magnitude. Note also that there is general reduction in the variance, but that the energetically best result does not guarantee the smallest variance.

Once more, for a detailed numerical analysis see our manuscript [12].

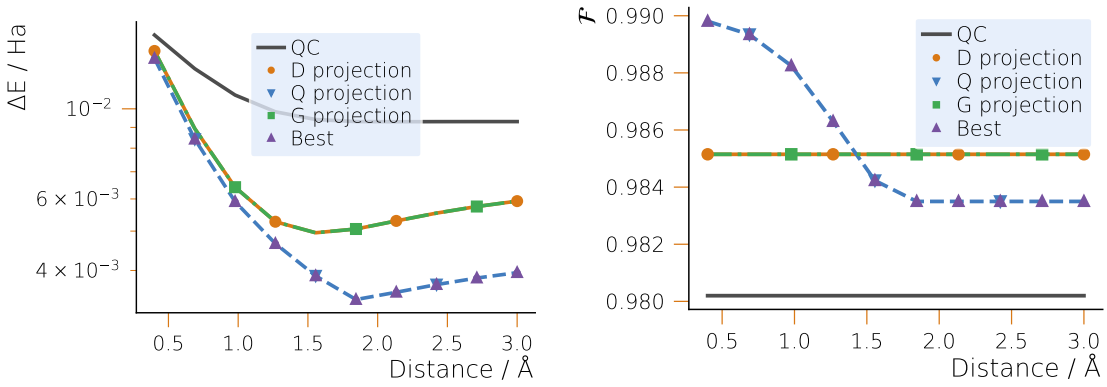

***Figure 6**: Energy difference w.r.t. the ground state and fidelity of the final state towards the exact ground state for H_2; directly from the quantum calculation (QC), the three individual projection in the particle, hole, or particle-hole sector (D, Q, or G) and the energetically best result (Best).*

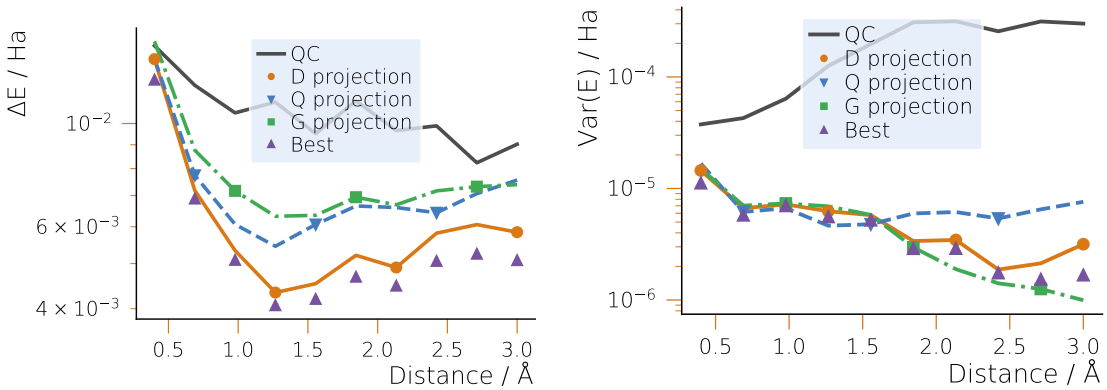

***Figure 7**: Energy difference w.r.t. the ground state and measurement variance for H_2; directly from the quantum calculation (QC), the three individual projection in the particle, hole, or particle-hole sector (D, Q, or G) and the energetically best result (Best).*

4 Adsorption of CO_2 on Graphene

In this chapter, we show the effort of TotalEnergies that continued their studies regarding benzene in deliverable D4.3, which also lead to a publication [6]. Here we present a calculation of a system of graphene and a CO_2 molecule using a VQE approach, which could be used in the context of understanding recapture processes of carbon dioxide. This chapter is a very brief summary of this study which is reported on in more detail in deliverable D4.8, with related software found on the NEASQC GitHub [13].

The setup of the graphene sheet and the CO_2 molecule is shown in Fig. 8. For the size of the graphene sheet we chose $n_x = 4$ and $n_y = 1$, and a parameterized distance of $\alpha \cdot 1.39\,\text{Å}$ between the atoms. As a basis for the system sto-3g was used, where we defined a small active space of 4 LUMO plus 4 HOMO, leading to calculations with 8 molecular orbitals that were mapped onto 16 qubits. The geometry relaxation using Hartree-Fock calculations to get initial values for α, θ, and ϕ was unfortunately ambiguous likely due to the small basis, hence, the values $\alpha = 1$, $\theta = 90°$, and $\phi = 0°$ were chosen to compare to results from literature (see hollow setup in Ref. [20]).

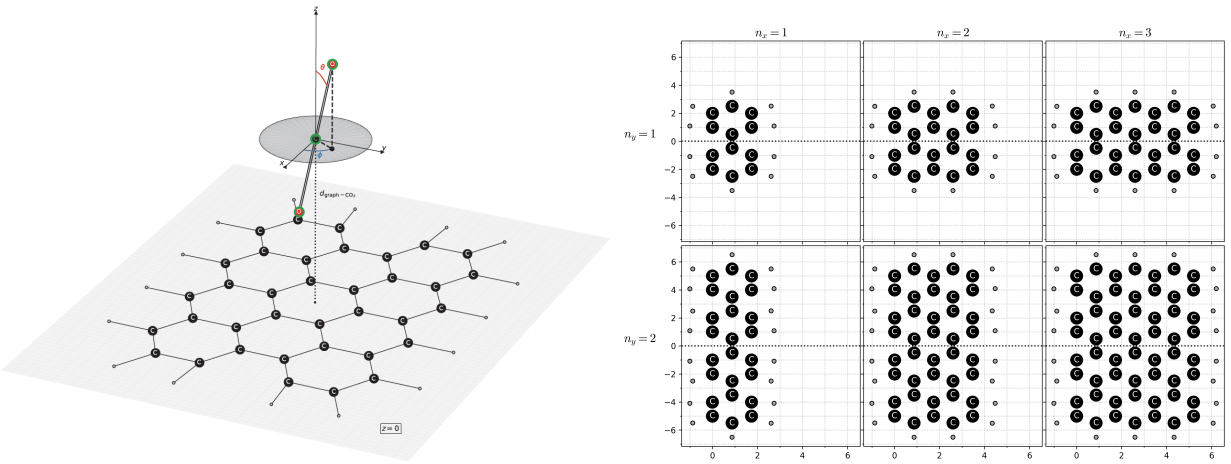

***Figure 8**: Geometry of the graphene plus CO_2 system with parameters for the orientation of the carbon dioxide molecule as well as the size of the graphene sheet.*

Fig. 9 shows results that can be obtained with our code: The qUCCSD energy and the exact energy, obtained with a full diagonalization of the active space Hamiltonians (FDASH) of 16 qubits. The main plot is the ground state energy as a function of $d_{\text{graph–CO}_2}$, while a sub-figure shows the dissociation energy $\Delta E = E - E[5\,\text{Å}]$ around 3.5 Å.

One can see that with 16 qubits, the ground state energy is minimal around 3.45 Å, which is slightly different from literature [20], where equilibrium distance is mostly between 3.38 Å and 3.40 Å, although it remains within the interval given in Table 2 of Ref. [20]. On the other hand, the exact binding energy of these 16 qubits systems is approximately $\Delta E \simeq 23\,\text{kJ} \cdot \text{mol}^{-1}$, which is consistent with experimental values [20, 21]; despite the choice of sto-3g as chemical basis set. Given that one can consider our geometry is between the 3'3-zigzag and the 5'3-armchair studied in Ref. [20], the exact binding energy obtained with 16 qubits Hamiltonians is significatively different from the values of Ref. [20], which can be explained by the difference of chemical basis set as well as the strong active space selection (from 422 qubits to 16 qubits).

On the qUCCSD side, the binding energy is approximately $\Delta E \simeq 23.3\,\text{kJ} \cdot \text{mol}^{-1}$, which is very close to the target. However, the shape of the curve between the minimal energy and the dissociation part is not exactly expected: We should reach smoothly an asymptotic when increasing $d_{\text{graph–CO}_2}$ instead of having a sudden jump in values. Furthermore, in CASCI calculations with larger active spaces of up to 16 HUMO plus 16 HOMO such a dissociation energy minimum could not be observed. This suggests that the basis choice is suboptimal, and it is likely that the active spaces are not large enough for the given problem. Additionally, we observed a very slow convergence for the qUCCSD runs, requiring over 10^4 iteration steps of the COBYLA optimizer to reach chemical precision, even in this small system (for larger systems this problem would worsen quickly). Overall, we conclude that this problem and concrete model seems not to be suited for NISQ devices, but our analysis inspires new directions of research that extend beyond the NEASQC project.

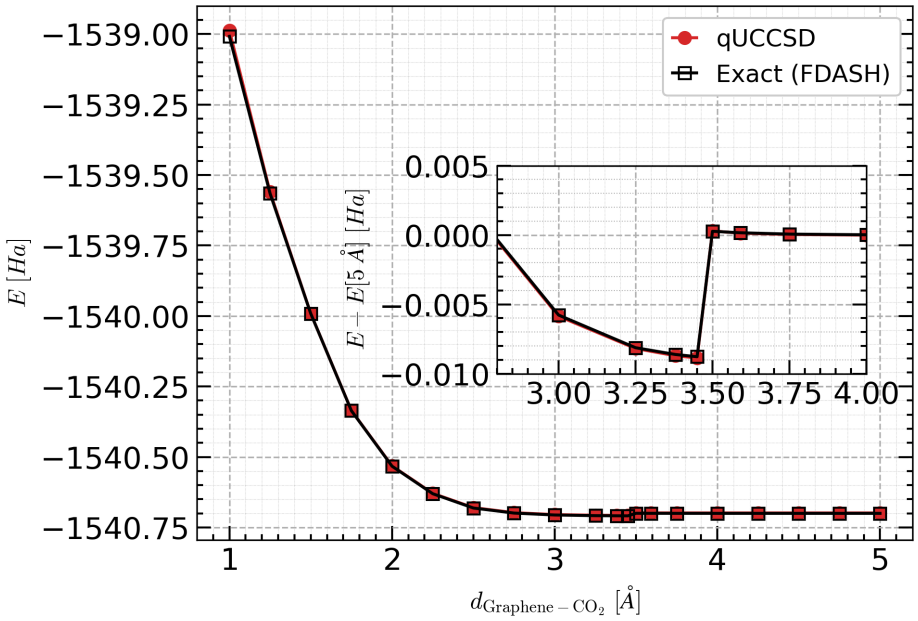

***Figure 9**: Ground state energy of the 16 qubits graphene plus CO_2 system as a function of $d_{graph-CO_2}$.*

5 KraChem for Automatic Subspace Generation (ASG)

Among the challenges one faces when working with NISQ devices are a limited number of available qubits and a limited quantum circuit depth. This in turn restricts the size of molecular systems that could be simulated on such machines.

ICHEC's software tool for automatic subspace generation, `KraChem` [14], is designed to automatically fragment molecular systems into smaller subsystems, allowing breaking down large problems into subproblems, making them digestible for NISQ computations. It was reported on in detail in deliverable D4.6, where the software itself can be found on the NEASQC GitHub [14].

5.1 About KraChem

`KraChem` is a Python library designed for working with chemical molecules, fragmentation, based on chemical files input and mathematical tools from graph theory.

The `KraChem` package has two main functionalities:

- Intermolecular fragmentation: Separation of two or more independent interacting moieties (typically two molecules). This find the collection of disconnected molecules in a given chemical compound.
- Intramolecular fragmentation: Separation of two or more moieties which belong to the same molecule, chain or system. This breaks a molecule into smaller parts, each of which is a collection of subsets of atoms, in a given molecule defined by its atoms and connections.

Although the fragmentation of a single molecule is a priori simple, the number of possible fragments increases exponentially with the number of atoms and is unviable for large systems. The AGS tool systematically explores, analyses and creates inter- and intra-molecular fragments keeping the chemical meaning, and provide with a full fragmentation scheme.

The `KraChem` library is implemented using Object-Oriented Programming (OOP), composed of the main class called *Molecule* and its methods and attributes.

5.2 Accessing and using KraChem

The `KraChem` library is available on the NEASQS GitHub as a repository at `https://github.com/NEASQC/qfrag/tree/master` [14].

A user guide is available in the form of a Jupyter notebook at `https://github.com/NEASQC/qfrag/blob/master/krachem_user_guide.ipynb` [14].

A set of input molecules that can be used as examples are provided at `https://github.com/NEASQC/qfrag/tree/master/input_molecules` [14].

5.3 Experiments and results

The `KraChem` repository also includes the following candidate input molecules and their fragmentation results:

- Benzene-CO_2
  - Input molecule file: `https://github.com/NEASQC/qfrag/blob/master/input_molecules/benzene_co2.sdf`
  - Fragmentation output files: `https://github.com/NEASQC/qfrag/tree/master/results/fragmentation_intra_benzene_co2`
- Caffine
  - Input molecule file: `https://github.com/NEASQC/qfrag/blob/master/input_molecules/caffeine.sdf`

- Fragmentation output files: https://github.com/NEASQC/qfrag/tree/master/results/fragmentation_leaves_caffeine

In summary, the package performs as expected and with good performance, meaning that in larger scale calculations, the fragmentation process would likely not be a bottleneck. Furthermore, while the process scales exponentially in principle, even for molecule sizes where the complete system represented in a basis to achieve reasonable accuracy would exceed the number of qubits currently available on NISQ devices ($\sim$ 100), `KraChem` should still be able to perform the fragmentation. This means the tool does indeed possess the means to make quantum chemical problems digestible for NISQ computers, which otherwise would not be simulatable.

5.4 Towards further benchmarking

The primary focus of Task 4.1 in the chemistry work package WP4 was to develop the ASG tool, which has been realized by ICHEC as `KraChem`, delivered in D4.6 of the project [14]. The second focus of Task 4.1 was for HQS to benchmark the fragmentation outputs using approximate classical methods to solve the whole problem and compare to the solutions from solving the fragments individually.

The second focus to benchmark the fragments requires a supporting theoretical framework to treat finite fragments in the presence of a surrounding molecular or bulk environment, which is not implemented within the scope of `KraChem` as defined in the work description. Consequently, the Task 4.1 team (ICHEC and HQS) have identified that one of the objectives beyond the NEASQC project in Task 4.1 or WP4 should be to expand `KraChem` to use methods such as the DMET methodology [22] to calculate the energy of each fragment and regenerate the total energy of the molecule studied. Furthermore, it will be of interest to incorporate this fragmentation scheme and DMET in the VQE-based quantum chemistry workflow that has been built in other use-case applications in WP4. A starting point for this will be to consider the QC-DMET [23, 24] code and PySCF to perform DMET calculations and integrate them within the `KraChem` code.

List of Figures

Bibliography

[1] NEASQC GitHub repository, *Variational Algorithms and Measurement Optimization*, https://github.com/NEASQC/Variationals_algorithms, 2024.

[2] A. Peruzzo, J. McClean, P. Shadbolt, M.-H. Yung, X.-Q. Zhou, P. J. Love, A. Aspuru-Guzik, and J. L. O'Brien, "A variational eigenvalue solver on a photonic quantum processor", en, Nature Communications **5**, 4213 (2014).

[3] H. R. Grimsley, S. E. Economou, E. Barnes, and N. J. Mayhall, "An adaptive variational algorithm for exact molecular simulations on a quantum computer", en, Nature Communications **10**, 3007 (2019).

[4] D. Wecker, M. B. Hastings, and M. Troyer, "Progress towards practical quantum variational algorithms", en, Physical Review A **92**, 042303 (2015).

[5] S. McArdle, T. Jones, S. Endo, Y. Li, S. C. Benjamin, and X. Yuan, "Variational ansatz-based quantum simulation of imaginary time evolution", en, npj Quantum Information **5**, 1–6 (2019).

[6] W. Sennane, J.-P. Piquemal, and M. J. Rančić, "Calculating the ground-state energy of benzene under spatial deformations with noisy quantum computing", en, Physical Review A **107**, 012416 (2023).

[7] NEASQC GitHub repository, *D4.2*, https://github.com/NEASQC/D4.2, 2022.

[8] A. Kovyrshin, M. Skogh, A. Broo, S. Mensa, E. Sahin, J. Crain, and I. Tavernelli, "A quantum computing implementation of nuclear-electronic orbital (neo) theory: toward an exact pre-born–oppenheimer formulation of molecular quantum systems", J. Chem. Phys. **158**, 214119 (2023).

[9] A. Kovyrshin, M. Skogh, L. Tornberg, A. Broo, S. Mensa, E. Sahin, B. C. B. Symons, J. Crain, and I. Tavernelli, "Nonadiabatic nuclear–electron dynamics: a quantum computing approach", J. Phys. Chem. Lett. **14**, 7065–7072 (2023).

[10] H. H. S. Chan, R. Meister, M. L. Goh, and B. Koczor, *Algorithmic shadow spectroscopy*, arXiv:2212.11036 (2022).

[11] G. Wang, D. E. Koh, P. D. Johnson, and Y. Cao, "Minimizing estimation runtime on noisy quantum computers", PRX Quantum **2**, 010346 (2021).

[12] T. Piskor, F. G. Eich, M. Marthaler, F. K. Wilhelm, and J.-M. Reiner, *Post-processing noisy quantum computations utilizing n-representability constraints*, arxiv:2304.13401 (2023).

[13] NEASQC GitHub repository, *D4.8*, https://github.com/NEASQC/D4.8, 2024.

[14] B. Chagas, G. Sánchez-Sanz, P. L. M. de Rituerto, and V. Kannan, "NEASQC D4.6 Automatic Subspace Generation (AGS) v1.0", https://github.com/NEASQC/qfrag/tree/master (2023).

[15] J. Dunning Thom H., "Gaussian basis sets for use in correlated molecular calculations. I. The atoms boron through neon and hydrogen", The Journal of Chemical Physics **90**, 1007–1023 (1989).

[16] G. M. J. Barca, C. Bertoni, L. Carrington, D. Datta, N. De Silva, J. E. Deustua, D. G. Fedorov, J. R. Gour, A. O. Gunina, E. Guidez, T. Harville, S. Irle, J. Ivanic, K. Kowalski, S. S. Leang, H. Li, W. Li, J. J. Lutz, I. Magoulas, J. Mato, V. Mironov, H. Nakata, B. Q. Pham, P. Piecuch, D. Poole, S. R. Pruitt, A. P. Rendell, L. B. Roskop, K. Ruedenberg, T. Sattasathuchana, M. W. Schmidt, J. Shen, L. Slipchenko, M. Sosonkina, V. Sundriyal, A. Tiwari, J. L. Galvez Vallejo, B. Westheimer, M. Wloch, P. Xu, F. Zahariev, and M. S. Gordon, "Recent developments in the general atomic and molecular electronic structure system", The Journal of Chemical Physics **152**, 154102 (2020).

[17] Q. Yu, F. Pavošević, and S. Hammes-Schiffer, "Development of nuclear basis sets for multicomponent quantum chemistry methods", J. Chem. Phys. **152**, 244123 (2020).

[18] A. Nyk anen, A. Miller, W. Talarico, S. Knecht, A. Kovyrshin, M. Skogh, L. Tornberg, A. Broo, S. Mensa, B. C. B. Symons, E. Sahin, J. Crain, I. Tavernelli, and F. Pavošević, "Toward accurate post-born–oppenheimer molecular simulations on quantum computers: an adaptive variational eigensolver with nuclear-electronic frozen natural orbitals", Journal of Chemical Theory and Computation **19**, 9269–9277 (2023).

[19] H.-Y. Huang, R. Kueng, and J. Preskill, "Predicting many properties of a quantum system from very few measurements", en, Nature Physics **16**, 1050–1057 (2020).

[20] C. Ehlert, A. Piras, and G. Gryn'ova, "CO_2 on Graphene: Benchmarking Computational Approaches to Noncovalent Interactions", en, ACS Omega **8**, 35768–35778 (2023).

[21] R. S. Smith and B. D. Kay, "Desorption Kinetics of Carbon Dioxide from a Graphene-Covered Pt(111) Surface", en, The Journal of Physical Chemistry A **123**, 3248–3254 (2019).

[22] G. Knizia and G. K.-L. Chan, "Density matrix embedding: a simple alternative to dynamical mean-field theory", Physical Review Letters **109** (2012).

[23] "QC-DMET: a python implementation of density matrix embedding theory for ab initio quantum chemistry", https://github.com/SebWouters/QC-DMET.

[24] Q. S. S. Wouters C. A. Jiménez-Hoyos and G. K. L. Chan, "A practical guide to density matrix embedding theory in quantum chemistry", Journal of Chemical Theory and Computation **12** (2016).